The dynamin-binding domains of Dap160/intersectin affect bulk membrane retrieval in synapses

Åsa M. E. Winther[1], Wei Jiao[1,*], Olga Vorontsova[1], Kathryn A. Rees[1], Tong-Wey Koh[2,‡], Elena Sopova[1], Karen L. Schulze[3], Hugo J. Bellen[2,3] and Oleg Shupliakov[1,§]

[1]Department of Neuroscience, DBRM, Karolinska Institutet, von Eulers väg 3, 171 77 Stockholm, Sweden
[2]Program in Developmental Biology, NRI, Baylor College of Medicine, Houston, TX 77030, USA
[3]Department of Molecular and Human Genetics and HHMI, NRI, Baylor College of Medicine, Houston, TX 77030, USA

*Present address: Center for Motor Neuron Biology and Disease, Columbia University Medical Center, New York, NY 10032, USA
‡Present address: Dept of Molecular, Cellular and Developmental Biology, Yale University, 266 Whitney Avenue, New Haven, CT 06511, USA
§Author for correspondence (oleg.shupliakov@ki.se)

Accepted 6 December 2012
Journal of Cell Science 126, 1021–1031

doi: 10.1242/jcs.118968

Summary

Dynamin-associated protein 160 kDa (Dap160)/intersectin interacts with several synaptic proteins and affects endocytosis and synapse development. The functional role of the different protein interaction domains is not well understood. Here we show that *Drosophila* Dap160 lacking the dynamin-binding SH3 domains does not affect the development of the neuromuscular junction but plays a key role in synaptic vesicle recycling. *dap160* mutants lacking dynamin-interacting domains no longer accumulate dynamin properly at the periactive zone, and it becomes dispersed in the bouton during stimulation. This is accompanied by a reduction in uptake of the dye FM1-43 and an accumulation of large vesicles and membrane invaginations. However, we do not observe an increase in the number of clathrin-coated intermediates. We also note a depression in evoked excitatory junction potentials (EJPs) during high-rate stimulation, accompanied by aberrantly large miniature EJPs. The data reveal the important role of Dap160 in the targeting of dynamin to the periactive zone, where it is required to suppress bulk synaptic vesicle membrane retrieval during high-frequency activity.

Key words: Scaffolding molecules, Protein migration, SH3 domain, Neuromuscular junction, *Drosophila*

Introduction

Clathrin-mediated endocytosis and bulk endocytosis are the two major pathways for synaptic vesicle (SV) recycling operating at the synaptic periactive zone (PAZ) (Saheki and De Camilli, 2012). The action of endocytic effector proteins executing these membrane trafficking events is coordinated by large scaffolding molecules, such as dynamin-associated protein 160 kDa, Dap160, in *Drosophila* (the mammalian ortholog is intersectin), and epidermal growth factor receptor pathway substrate clone 15, Eps15. Both proteins act as a molecular scaffold and their loss leads to very similar defects in endocytosis *in vivo* (Koh et al., 2007). Experiments in non-neuronal cells have shown that they are localized at endocytic sites via binding to F-bar proteins, FCHo1 and 2 (Henne et al., 2010) and act as a platform to recruit endocytic effectors implicated in regulation of the actin cytoskeletal network at the presynaptic membrane. Although significant progress has been made in the identification of the binding partners of the scaffolding proteins, their precise function in synapses is poorly understood (Dittman and Ryan, 2009; Pechstein et al., 2010).

One of the key endocytic effector proteins implicated in interactions with the scaffolding protein complex is the GTPase dynamin, encoded by the gene *shibire* (*shi*) in flies (Evergren et al., 2007; Koh et al., 2004; Marie et al., 2004; Roos and Kelly, 1998). Dynamin is part of the protein machinery that mediates fission of newly formed vesicles from the plasma membrane. In temperature sensitive shi^{ts1} mutants kept at the restrictive temperature, most SVs fuse with the presynaptic membrane, but endocytosis is blocked and endocytic intermediates with dynamin collars and large vacuoles accumulate. Genetic deletion of all three mammalian dynamin genes also results in a block of synaptic vesicle recycling and accumulation of numerous constricted coated pits (Ferguson and De Camilli, 2012).

Interactions with dynamin involve several Src homology (SH3) domain modules of Dap160/intersectin (Roos and Kelly, 1998). In *Drosophila* nerve terminals this binding has been proposed to be important for aspects of dynamin function (Broadie, 2004; Koh et al., 2004; Marie et al., 2004; Roos and Kelly, 1998). Surprisingly, the complete loss of *dap160* causes phenotypes in neuromuscular junctions (NMJs) that are much less severe than the loss of dynamin (Koh et al., 2004; Marie et al., 2004). Low frequency nerve stimulation results in near normal EJPs in *dap160* mutants. Only conditions of high-frequency activity, such as 10 minutes of 10 Hz stimulation, revealed impairments in synaptic transmission (Koh et al., 2004). Similarly, assays of synaptic vesicle endocytosis with FM dye loading revealed no short-term defects in *dap160* mutants, although after a 10-minute labeling period, dye uptake was significantly reduced (Marie et al., 2004). However, the *dap160* null mutants displayed twofold higher frequency of spontaneous activity and larger amplitude of spontaneous events. Up to 50% decrease in levels of several endocytic proteins, including dynamin, endophilin, and synaptojanin was also reported (Koh et al., 2004; Marie et al., 2004). These findings led to the suggestion that Dap160 may coordinate the function of endocytic proteins at the PAZ, but they did not explain how it fulfilled this function.

In the present study we investigate how Dap160 may coordinate dynamin functions at the PAZ. We used the *dap160* null background to express mutant Dap160 proteins lacking dynamin-interacting modules in neurons in order to study its function. Our experiments show that Dap160 relocates from the vesicle pool to the periactive zone during synaptic activity and that it concentrates dynamin at the PAZ. The interaction between the two proteins plays an essential role in controlling bulk SV membrane trafficking at the NMJ, but is not critical for clathrin-mediated endocytosis.

Results

Dap160 accumulates in the distal pool of synaptic vesicles at rest and relocates to the PAZ during synaptic activity

We first investigated the localization of Dap160 and its binding partner, dynamin, at rest and during synaptic activity following exposure to 60 mM K^+ (high K^+) for 10 minutes using confocal microscopy (Fig. 1A). Both proteins strongly colocalized under both conditions (Fig. 1B). A redistribution of the proteins within nerve terminals under stimulation was evident in confocal images (Fig. 1A). To examine their distribution within the active zone, we double-stained NMJs with antibodies against Dap160 and the presynaptic T-bar component, Bruchpilot (Brp) (Fig. 1C,D). The Brp labeling accumulated in spots, which indicated the position of the T-bar (Wagh et al., 2006). The size of individual punctae remained unchanged both at rest and upon high K^+ stimulation (supplementary material Fig. S1A), while the level of colocalization between Dap160-ir and Brp-ir significantly decreased in stimulated synapses (Fig. 1D). The Dap160-ir accumulated in clear circles around Brp spots (Fig. 1C). Such 'circles' have been observed previously and are thought to outline synaptic periactive zones (Marie et al., 2004; Roos and

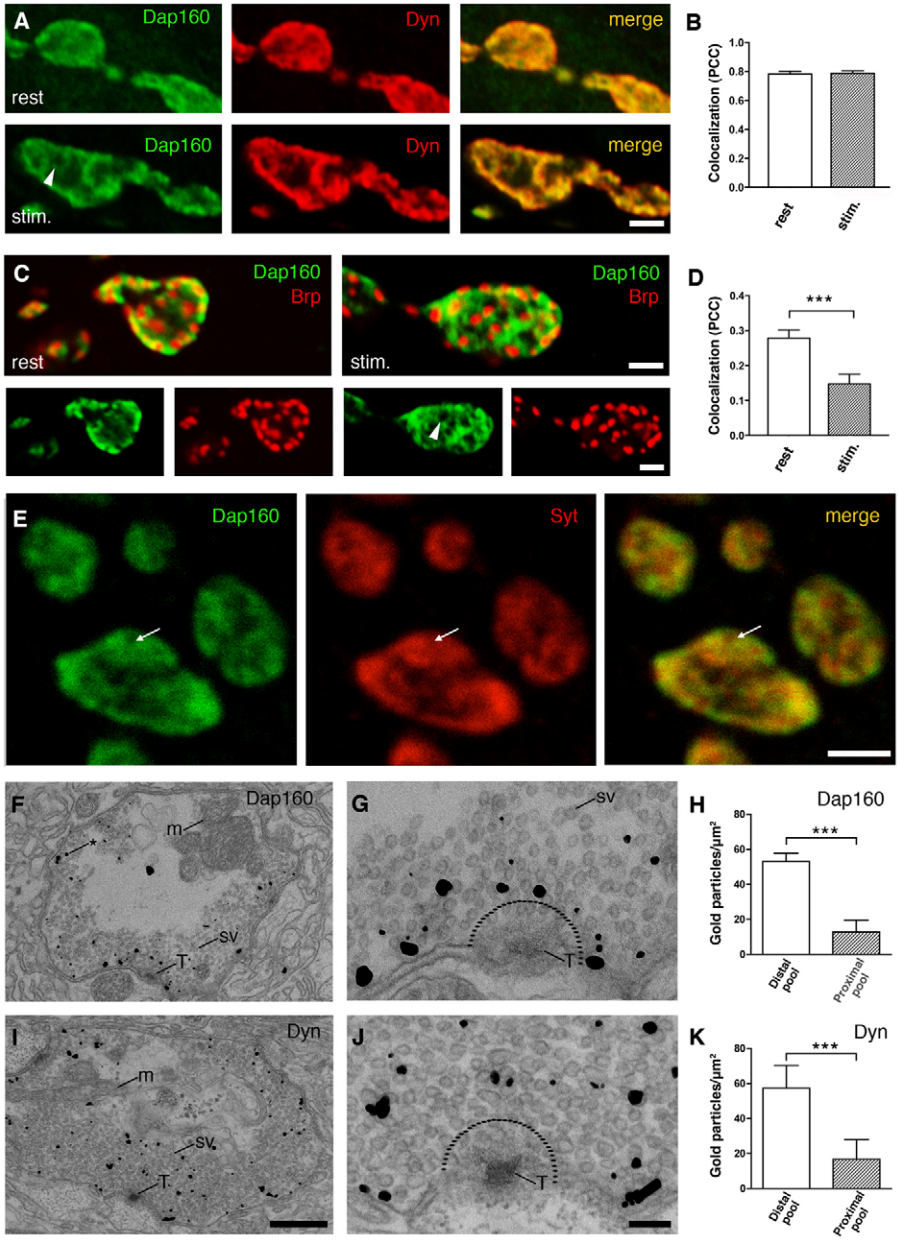

Fig. 1. Localization of Dap160, dynamin and Bruchpilot in control (w^{1118}) third instar NMJs. (**A**) Confocal images of NMJs double-labeled for Dap160 (green) and dynamin (Dyn, red) at rest and upon exposure to high K^+ for 10 minutes (stim). Arrowheads indicate unlabeled areas in boutons induced by stimulation. (**B**) Quantification of the colocalization of dynamin and Dap160 at rest and following stimulation, as measured by Pearson's correlation coefficient (PCC). (**C**) Confocal images showing optical middle sections of boutons double-labeled for Dap160 (green) and Bruchpilot (Brp, red) at rest and upon high K^+ stimulation. Dap160-ir often surrounds the areas labeled by anti-Brp, but some degree of colocalization is observed. (**D**) Quantification shows that the colocalization between Dap160 and Brp decreases upon stimulation. (**E**) Confocal microscopy image of an NMJ double-labeled for Dap160 (green) and synaptotagmin (Syt, red). Arrows indicate an area in which Dap160 is not overlapping with Syt. (**F**,**G**,**I**,**J**) Dap160 and dynamin are concentrated to the distal pool of synaptic vesicles at rest. (F,I) Low magnification electron micrographs from immunogold-labeled NMJs showing the distribution of Dap160-ir (F) and dynamin-ir (I). Asterisk in F indicates a silver-enhanced gold particle. (G,J) High-magnification images of Dap160-ir (G) and dynamin-ir (J). Dashed outlines correspond to the border of the proximal pool of vesicles. (**H**,**K**) Bar graphs showing densities of gold particles (particles/µm^2) in the distal and proximal pools of synaptic vesicles for Dap160 (H) and dynamin (K). T, T-bar; m, mitochondrion; sv, synaptic vesicle. Bar graphs indicate mean + s.e.m. ***$P<0.001$ using Student's *t*-test. Scale bars: 2 µm (A,C,E); 0.5 µm (F,I); 0.1 µm (G,J).

Kelly, 1998; Roos and Kelly, 1999). This suggests that both Dap160 and dynamin relocate from an undefined synaptic compartment to the PAZ upon stimulation.

To define this compartment we studied the subcellular localization of Dap160 at rest using stimulated emission depletion (STED) microscopy (supplementary material Fig. S1B–D). Serial STED images through NMJs show that Dap160 surrounds unlabeled areas of the bouton located at or close to the plasma membrane (supplementary material Fig. S1C,D). We then labeled NMJs for synaptotagmin, a SV-associated protein (Estes et al., 1996; Littleton et al., 1993), to determine if Dap160 colocalizes with a SV marker. Synaptotagmin and Dap160 are largely overlapping but do not completely colocalize, and punctae labeled only with synaptotagmin are clearly seen (Fig. 1E). This further suggests that Dap160 at rest localizes in the intravesicular matrix within the SV pool (Pechstein et al., 2010).

We next used electron microscopy (EM) in conjunction with the immunogold technique to further clarify the subcellular localization of Dap160 and dynamin. The gold particles were silver enhanced to improve visualization of the labeling at the EM level. Dap160 and dynamin were found in the pool of SVs more than 100 nm away from the borders of the T-bar pedestal (Fig. 1F–K). The SVs immediately surrounding the presynaptic T-bar were not labeled (Fig. 1G,H,J,K; supplementary material Fig. S2A). To confirm that these vesicles and structures surrounding the T-bar are accessible to labeling with our immunogold approach we stained the NMJs with antibodies against cysteine string protein, CSP (Zinsmaier et al., 1994), and Brp (Wagh et al., 2006) (supplementary material Fig. S2B–F). As expected the gold particles labeling CSP were evenly distributed throughout the whole pool of SVs (supplementary material Fig. S2D–F). The antibody raised against the C-terminus of Brp labeled the filaments emerging from the T-bar (supplementary material Fig. S2B,C). The labeling patterns of CSP and Brp demonstrate that the T-bar and its immediate surroundings are accessible for immunolabeling, and our experiments localize Dap160 and its binding partner dynamin to the distal pool of SVs.

To determine how the localization of Dap160 and its binding partner dynamin change during synaptic activity, we fixed NMJs after exposure to high K^+ for 10 minutes and stained using the immunogold technique and found labeling close to the plasma membrane in PAZs (Fig. 2A,B). To verify that the proteins are localized in the PAZ at the EM level we also stained shi^{ts1} mutants exposed to the restrictive temperature (29˚C) for 10 minutes, in which the synaptic vesicle recycling machinery is ‘locked’ at the PAZ (Koenig and Ikeda, 1989) (Fig. 2C,D). In agreement with immunofluorescence data, both in control and shi^{ts1} presynaptic terminals, Dap160 and dynamin were found concentrated in the PAZ (Fig. 2A–I). Quantification of gold particle densities revealed a significant increase in Dap160 and dynamin labeling in this region (Fig. 2H,I). Interestingly, although many control terminals still contained numerous synaptic vesicles, the majority of the gold particles were concentrated at the plasma membrane, suggesting that the proteins were not bound to SVs during neurotransmitter release and migrated to the periactive zone via an independent pathway (Fig. 2A,B). In shi^{ts1}mutants almost all gold particles were associated with the membrane regions containing constricted collared pits at the plasma membrane, consistent with a role of Dap160 and dynamin in endocytosis (Fig. 2C,D).

We then reconstructed immunogold-particle localization at release sites for Dap160 in 3D from serial ultrathin sections of NMJs at rest and during synaptic activity in control and shi^{ts1}mutant (Fig. 2E–G; supplementary material Fig. S2G–I). In resting control synapses only 10% of gold particles were in the PAZ, while 70% were in the PAZ in stimulated controls, and 90% in stimulated shi^{ts1}mutants. Taken together, these experiments show that Dap160 and its binding partner dynamin relocate from the distal vesicle pool region to the PAZ during synaptic activity.

Deletion of Dap160 results in the mislocalization of dynamin but not Eps15 from the PAZ

We then assessed dynamin distribution in *dap160* null mutants, $dap160^{\Delta 1}/Df(2L)bur\text{-}K1$ (Koh et al., 2004), at rest and during synaptic activity. Immunofluorescence and immunogold EM experiments show that dynamin distribution is not dramatically changed in mutants when compared to control at rest (Fig. 3A,G). Dynamin is associated with the vesicle pool at rest and it is largely colocalized with Eps15 and the endocytic adaptor complex, AP2 (Fig. 3A–C,G,I; supplementary material Fig. S3A,C). At the EM-level, in *dap160* null mutants at rest, a decrease in dynamin gold particle density is detected at the PAZ compared to control (Fig. 3K–M,P; $P<0.05$), whereas no decrease is observed for Eps15 labeling versus control (supplementary material Fig. S3D).

In stimulated *dap160* null mutant NMJs, dynamin is dispersed throughout the terminal and is no longer accumulated in spots of fluorescence at the PAZ, unlike in stimulated control NMJs (Fig. 3D,H). However, Eps15 is still localized to endocytic punctae and colocalizes with AP2 as in control and shi^{ts1} NMJs (Fig. 3E,F,J; supplementary material Fig. S3B,C). Immunogold EM experiments confirmed that dynamin is not concentrated at the PAZ and is distributed along the presynaptic membrane in *dap160* mutant NMJ boutons (Fig. 3N,O). Quantification of gold particles showed a relative reduction of dynamin immunolabeling in the PAZ compared to stimulated control (Fig. 3Q). When compared to stimulated shi^{ts1}, the percentage of endocytic pits at the PAZ associated with dynamin-immunoreactive gold particles was reduced threefold (from 72.7±24.9%; $n=19$ to 23.7±26.3%; $n=15$; mean±SD, $P<0.0001$, Student’s *t*-test). The relative distribution of gold particles for Eps15 was not significantly different comparing stimulated control, *dap160* and shi^{ts1} animals (supplementary material Fig. S3E). Hence, deletion of *dap160* leads to a specific mistargeting of dynamin from the PAZ during stimulation.

Dynamin is mislocalized from the PAZ in a *dap160* mutant lacking the dynamin-interacting SH3 domains

Genetic deletion of *dap160* results in a decrease of about 50% of the levels of several endocytic proteins, including dynamin, as well as to the appearance of satellite boutons, indicating a developmental defect (Koh et al., 2004; Marie et al., 2004). To investigate the functional role of dynamin targeting to the periactive zone by Dap160, we generated *dap160* mutants lacking the dynamin interacting modules. To accomplish this, we first confirmed the earlier observations of Roos and Kelly (Roos and Kelly, 1998) that only the SH3A and SH3B domains bind dynamin (Fig. 4A). GST pull-down experiments with various SH3 domain combinations of Dap160 showed that SH3B is the key dynamin binding module (Fig. 4A). SH3AB and

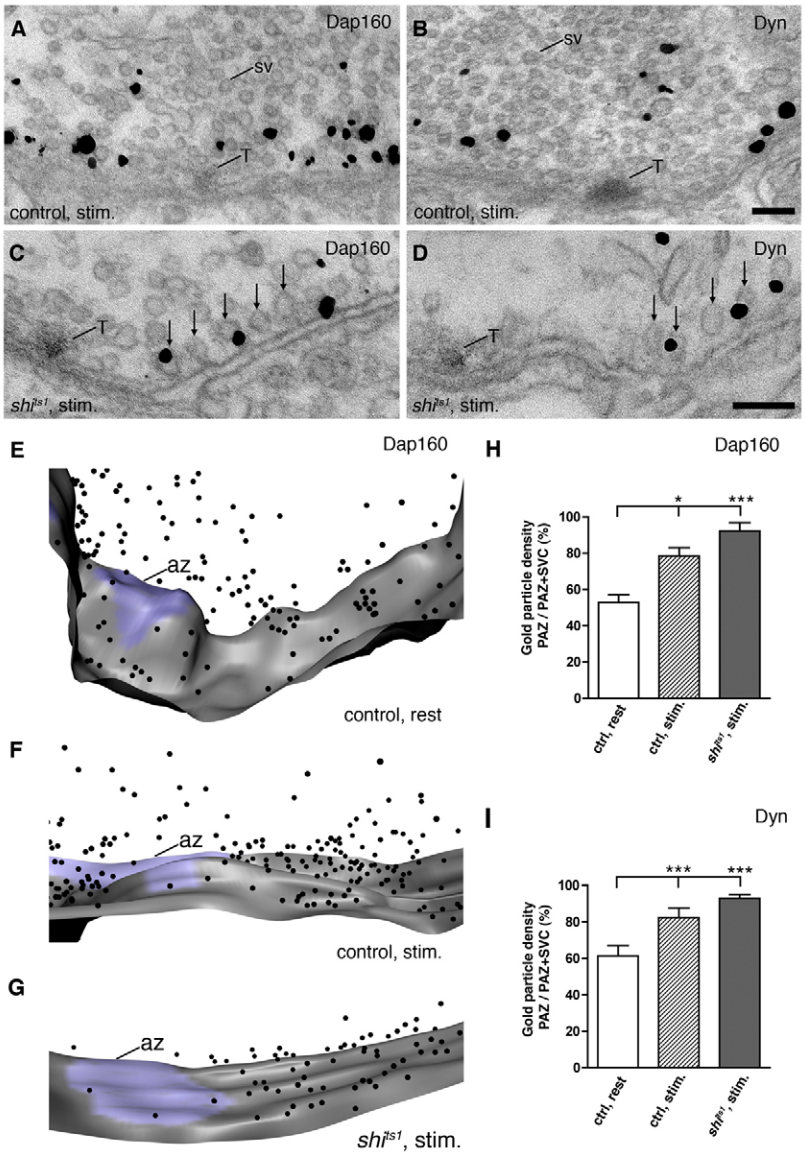

Fig. 2. Stimulation causes redistribution of Dap160 and dynamin to the periactive zone. (**A**,**B**) Electron micrographs of nerve terminals of control third instar larvae control after exposure to high K^+ for 10 minutes showing an accumulation of Dap160-ir and dynamin-ir (Dyn) at the periactive zone. (**C**,**D**) High-magnification images showing that Dap160-ir and dynamin-ir are associated with invaginated endocytic pits accumulated at the plasma membrane in stimulated *shi*^{ts1} nerve terminals. Arrows indicate endocytic intermediates. (**E**–**G**) 3D reconstructions of the subcellular localization of Dap160-ir in synapses. Plasma membrane is depicted gray, active zones are violet. Silver-enhanced immunogold particles are shown as black spheres. Eight active zones were studied in serial sections for each case. (**H**,**I**) Bar graphs showing the relative distribution of gold particles to the periactive zone upon stimulation. Bar graphs indicate mean + s.e.m. *$P<0.05$; ***$P<0.001$ using ANOVA, Tukey's post test. Scale bars: 0.1 μm.

SH3A-D displayed stronger binding than SH3B alone, suggesting cooperativity among the SH3 domain modules. We then created transgenics in the *dap160*$^{\Delta 1}$*/Df(2L)bur-K1* null background and expressed them using the GAL4/UAS system and a neural-specific GAL4 driver (elav-GAL4^{C155}). Two *dap160* transgenes were generated, one lacking the SH3B domain (ΔB) and the other lacking both SH3A and SH3B domains (ΔAB). Animals that expressed the full-length *dap160* cDNA under UAS control served as a positive control (Fig. 4B). The full-length and mutated *dap160* transgenes rescued the lethality of *dap160*$^{\Delta 1}$*/Df(2L)bur-K1* mutants to viable adults, which were fertile and able to fly. From here onwards, *ΔB* and *ΔAB* refers to animals that express the respective mutated *dap160* transgenes in the *dap160* null mutant background. We then confirmed that GST-bound dynamin proline-rich domain (PRD) does not immunoprecipitate Dap160 lacking SH3A and SH3B domains from the head extracts of our mutant transgenics, whereas it successfully precipitated Dap160 in wild-type and full-length rescue controls (supplementary material Fig. S4A). A weak Dap160 band was still detectable in case of *ΔB*. A locomotion assay performed at 25°C did not reveal significant motor defects in *ΔAB* third instar larvae. However, a large decrease in locomotor activity was observed in *dap160* null mutants (Fig. 4G). Under stress conditions at elevated temperature (34°C), at which the temperature-sensitive null mutant is paralyzed, a locomotion defect in *ΔAB* significantly different from controls was observed, suggesting a synaptic defect (Fig. 4H).

Earlier studies have revealed severe developmental defects in the synaptic architecture of *dap160* null mutants (Koh et al., 2004). It is possible that delivery of dynamin to nerve terminals by Dap160 is important for synaptic development. However, the *ΔAB* mutant, which lacks dynamin-interacting modules, did not display any defects in synaptic architecture or changes in number of satellite boutons (Fig. 4C–F). In addition, immunofluorescence did not reveal significant differences in dynamin expression in NMJs in the *ΔAB* mutant compared to control (supplementary material Fig. S4B–E). Thus, interactions of Dap160 involving

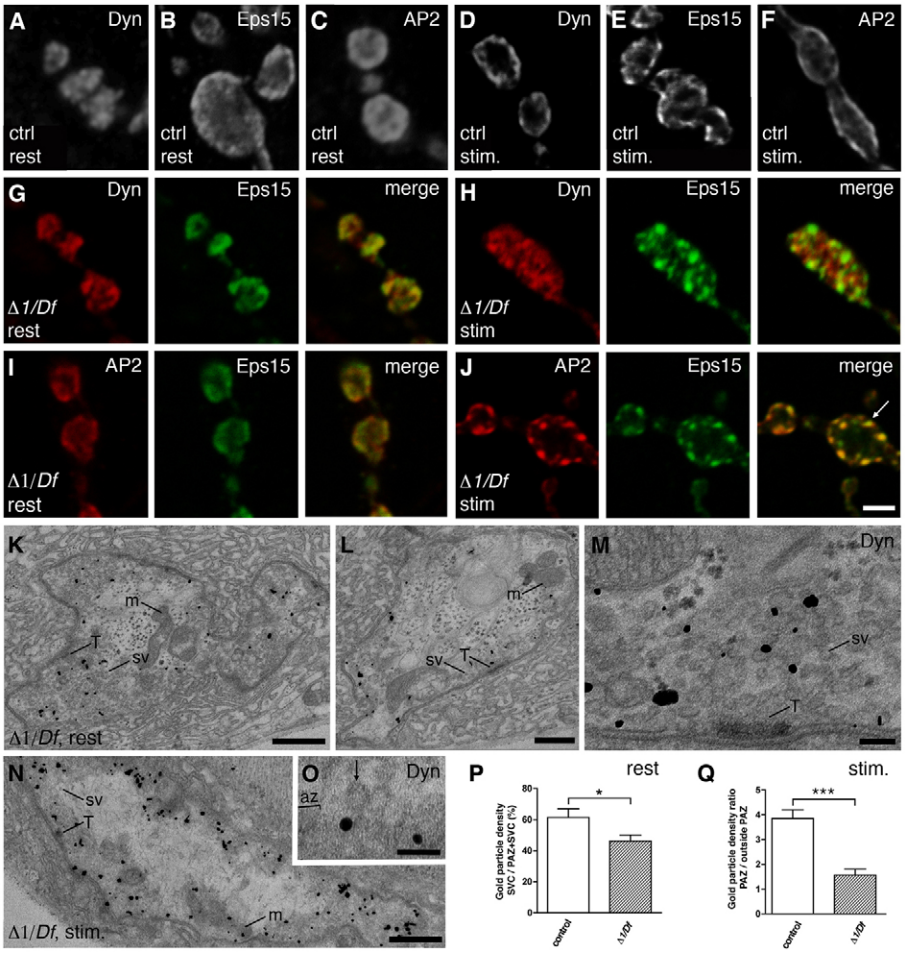

Fig. 3. Mislocalization of dynamin from the periactive zone in the *dap160* mutant (Δ1/Df). (**A–C**) Confocal microscopy images showing the localization of (A) dynamin (Dyn), (B) Eps15 and (C) AP2 at rest in control NMJs. (**D–F**) Following stimulation there is a redistribution of (D) dynamin-ir, (E) Eps15-ir and (F) AP2-ir in control boutons. (**G**,**H**) Confocal images of *dap160* mutant NMJs showing that Dyn (red) and Eps15 (green) are largely colocalized at rest and have similar distribution (G). During stimulation, dynamin is no longer accumulated in spots, unlike Eps15 (H). (**I**,**J**) Confocal images showing AP2-ir (red) and Eps15-ir (green) in *dap160* mutant nerve terminals at rest (I) and after stimulation (J). Note colocalization of both proteins in spots at the plasma membrane (arrow). (**K**,**L**) Low magnification electron micrographs illustrating the overall view of dynamin immunolabeling in *dap160* mutant NMJs at rest. (**M**) High-magnification image showing dynamin-ir within the SV pool in *dap160* mutant at rest. (**N**) Mistargeting of dynamin in the mutant NMJ upon stimulation. (**O**) High-magnification image of a labeled constricted pit (arrow) accumulated at the periactive zone following high K^+ stimulation. (**P**,**Q**) Quantification of dynamin localization in the synaptic vesicle pool (rest) and at the PAZ (stim) in control and *dap160* mutant. Bar graphs indicate mean + s.e.m. *$P<0.05$; ***$P<0.001$ using Student's *t*-test. T, T-bar; m, mitochondrion; sv, synaptic vesicle; az, active zone. Scale bars: 2 µm (A–J); 0.5 µm (K,L); 0.1 µm (M); 0.2 µm (N); 50 nm (O).

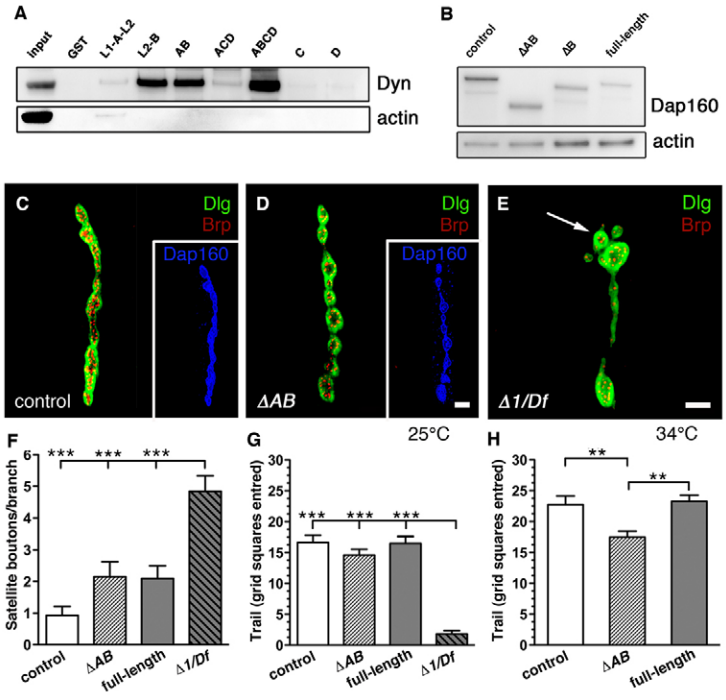

Fig. 4. Properties of the *ΔAB* mutant. (**A**) GST-fusion proteins containing Dap160-SH3A and/or SH3B precipitate dynamin from w^{1118} head extracts, whereas GST-SH3C, GST-SH3D and GST alone do not. Note that SH3AB and SH3A-D precipitate larger amounts. Precipitated proteins were subjected to western blotting with anti-dynamin and anti-actin. 1% of the extract used for the pull-down assay was loaded for lane 1 (Input). L1, linker region N-terminally of SH3A; L2 linker region between SH3A and B. (**B**) *dap160* mutant flies expressing different UAS-*dap160*-rescue constructs (*ΔAB*, lacking SH3A and B; *ΔB*, lacking SH3B and full-length rescue) pan-neuronally produce Dap160, as revealed by western blot of head extracts stained with antibodies against Dap160 and actin. (**C**,**D**) Confocal images of NMJ4 stained with anti-Dlg (green) to reveal bouton outlines, anti-Brp (red) to reveal presynaptic active zones and anti-Dap160 (blue, insets). Normal NMJ morphology is seen in control larva (C) and in NMJs from *ΔAB* mutant (D). (**E**) Satellite boutons are apparent in the *dap160* null mutant (Δ1/Df), arrow indicates example of one satellite bouton. (**F**) Quantification of the number of satellite boutons in the different *dap160* rescue lines compared with control and *dap160* null mutant. There were no significant differences between the numbers of satellite boutons in control, *ΔAB* and full-length rescue larvae. (**G**) Locomotion behavior in *dap160* null mutant is significantly different from that of control, *ΔAB* and full-length rescue at 25°C. (**H**) At 34°C, a significant reduction (~24%) in grid squares entered was detected in *ΔAB* compared to control and full-length rescue larvae. Temperature-sensitive *dap160* null mutant does not move at 34°C (not shown). Bar graphs indicate mean + s.e.m. **$P<0.01$, ***$P<0.001$ using ANOVA, Tukey's post test. Scale bars: 2 µm (C–E).

other portions than the SH3A-B module can successfully control the dynamin transport to the nerve terminal during development.

In resting synapses of both *ΔB* and *ΔAB* larvae, there were no significant differences in localization of dynamin. As in control, a strong colocalization with Eps15 was observed (Fig. 5A,C,E). However, upon stimulation with high potassium, dynamin is mislocalized. Confocal images of *ΔAB* larvae clearly show that dynamin immunoreactivity is no longer concentrated in spots at the PAZ, in contrast to control NMJs (Fig. 5B,D,E). Mistargeting of dynamin in stimulated *ΔB* mutant synapses was also evident, but less pronounced (Fig. 5E). To test if targeting of Dap160$^{\Delta AB}$ to the PAZ during stimulation is perturbed in *ΔAB* mutants, we double-stained stimulated NMJs with antibodies raised against AP2 and the EH domain region of Dap160. Strong colocalization of Dap160$^{\Delta AB}$ and AP2 in spots of fluorescence was observed indicating that Dap160$^{\Delta AB}$ relocate along with AP2, as observed in control (Fig. 5F,G). Taken together, these experiments indicate that dynamin-interacting domains of Dap160 are predominantly responsible for targeting and accumulating dynamin at sites of synaptic vesicle recycling in *Drosophila* NMJs upon intense stimulation.

Synaptic transmission and styryl dye uptake in NMJs in Dap160 mutants lacking dynamin-interacting domains is impaired

Earlier experiments revealed defects in synaptic transmission in *dap160* null mutants and showed that they can be restored in animals expressing the full-length rescue construct (Koh et al., 2004; Marie et al., 2004). The defects are temperature dependent. The major physiological defects at room temperature (22°C) included an increase in average amplitude of miniature junction potentials (mEJPs) and a decrease in amplitude of EJPs after prolonged high-frequency stimulation at 10 Hz. To determine whether neurotransmitter release is perturbed in transgenic *ΔAB* animals, we recorded in 1 mM Ca^{2+} and observed no significant difference in the amplitude and frequency of spontaneous mEJPs (Fig. 6A–C). The amplitude of evoked EJPs recorded at 0.3 Hz was also not significantly altered (Fig. 6D,E).

We then determined whether *dap160$^{\Delta AB}$* NMJs can sustain high-frequency neurotransmitter release. Muscles 6/7 were stimulated at 10 Hz for 10 minutes. The recorded data were binned at 60-second intervals and normalized to the first EJP amplitude bin. The *dap160$^{\Delta AB}$* synapses show a significant decrease in average EJP amplitude during stimulation when compared to the control (Fig. 6F). A similar decrease in average EJP amplitude during high-frequency stimulation has been observed in our previous studies in null mutants (Koh et al., 2007).

To study the recovery from synaptic depression, NMJs were stimulated for 4 minutes at 10 Hz and then single stimuli delivered at 0.3 Hz to measure the recovery. EJPs amplitudes in *dap160$^{\Delta AB}$* rescue mutants recover to the original level in less than 5 minutes and at a much slower rate than control (supplementary material Fig. S5A). Interestingly, large amplitude spontaneous events were observed during the recovery phase following high-frequency stimulation, some of which reached up to 11.2 mV (Fig. 6G,H). These large fusion events disappeared 60 seconds after the stimulation (Fig. 6I). Hence, the data indicate that dynamin binding domains are necessary to maintain normal synaptic transmission. Slow recovery and presence of large spontaneous events following high-frequency stimulation suggest a defect in endocytosis and/or the release machinery in the synapse during and briefly after high-frequency activity.

To further assay the observed defect in synaptic transmission we assessed loading of the styryl dye FM1-43 in control, *ΔAB*, *shi^{ts1}* and full-length *dap160* rescue third instar larvae using a standard protocol (Verstreken et al., 2008). We observed a statistically significant decrease in FM1-43 loading in the *ΔAB* animals as compared to control and full-length rescue

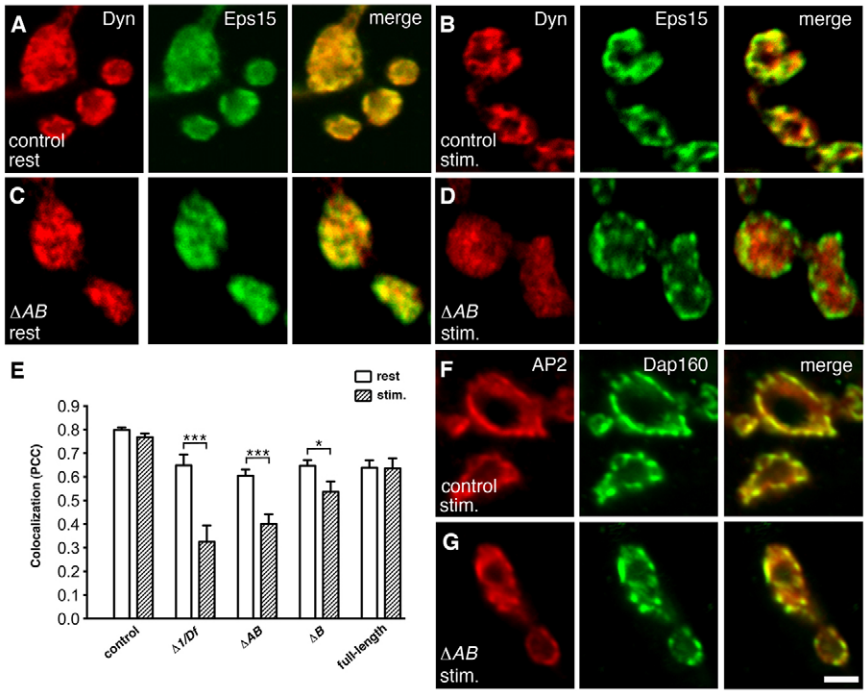

Fig. 5. SH3A and B domains of Dap160 are required for correct dynamin targeting during synaptic activity. (**A**–**D**) Confocal microscopy images of nerve terminals fixed at rest and upon high K^+ stimulation labeled with antibodies against dynamin (Dyn) and Eps15. (A,B) In control larvae, dynamin-ir and Eps15-ir are largely colocalized and, following stimulation, concentrated to spots close to the perimeter of the bouton. (C,D) Nerve terminals of larvae expressing the *Δ*AB-rescue construct. After stimulation, dynamin-ir is not concentrated to spots and is dispersed in the bouton. (**E**) Quantification of colocalization of dynamin-ir and Eps15-ir in boutons from control, *dap160* null (Δ1/Df) and different rescue lines, at rest and upon stimulation. Lower colocalization level in full-length rescue compared to control is possibly due to slightly lower level of Dap 160 expression in the rescue mutant. Colocalization is measured as Pearson's correlation coefficient (PCC). (**F**,**G**) Confocal microscopy images of control (F) and *ΔAB* (G) nerve terminals labeled with anti-α-adaptin (AP2) and anti-Dap160 after stimulation. In both control and *ΔAB*, labeling is mostly colocalized and concentrated to spots. Bar graphs indicate mean + s.e.m. *$P<0.05$; ***$P<0.001$ using Student's *t*-test. Scale bar: 2 μm.

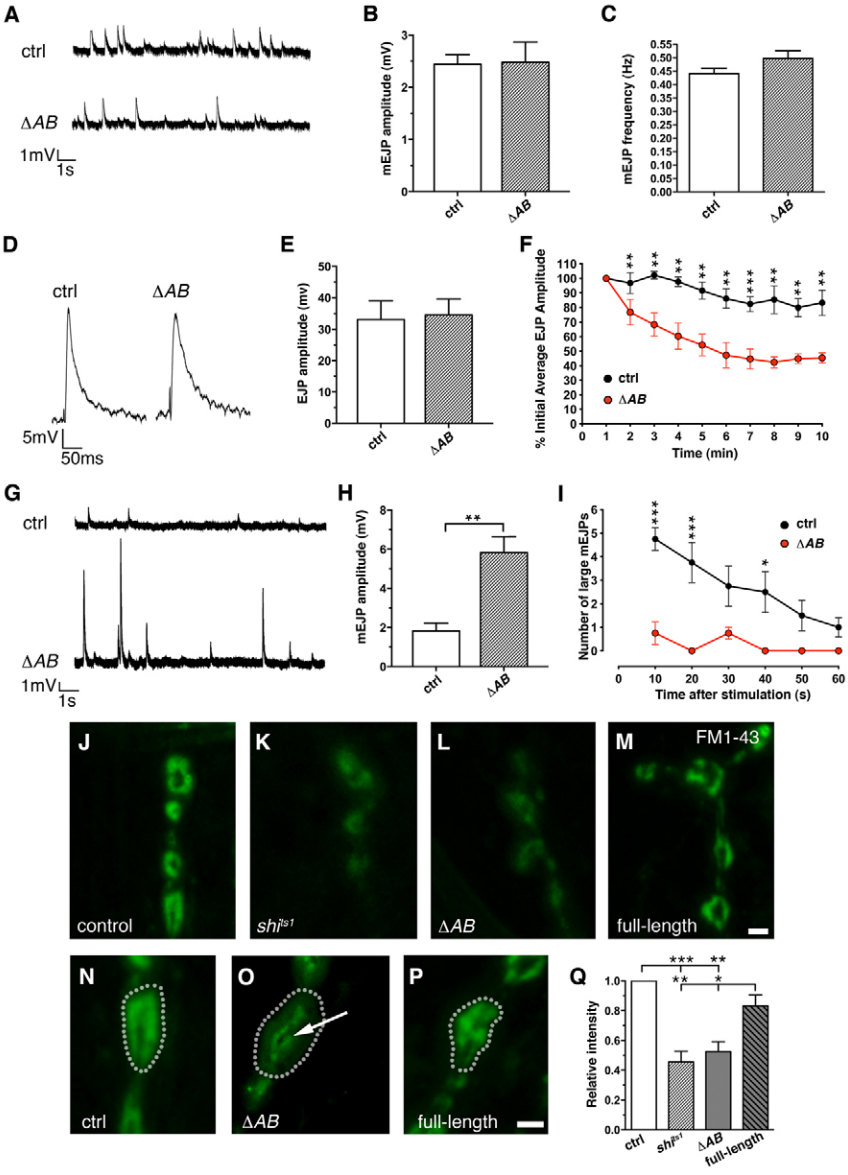

Fig. 6. Synapses in *ΔAB* mutant show synaptic depression at high-frequency stimulation followed by large mEJPs during recovery phase, as well as decreased membrane uptake upon stimulation. (**A**) Example traces for mEJPs recorded from muscle 6 of control and *ΔAB* NMJ. (**B**,**C**) Histograms showing the average amplitude and frequency of mEJPs. Control and *ΔAB* do not show a significant difference in EJP amplitude or frequency. (**D**) Example traces of the evoked EJPs induced by 0.3 Hz stimulations. (**E**) Bar graph showing average amplitude EJPs recorded at 0.3 Hz. (**F**) When stimulated at 10 Hz, *ΔAB* NMJs show synaptic depression. Evoked amplitude at high-frequency stimulation for 10 minutes, normalized to the first EJP amplitude. (**G**) Traces showing examples of large mEJPs recorded from ΔAB during the first 15 seconds following 10 minutes of 10 Hz stimulation. mEJPs recorded from control are normal. (**H**) Histogram showing the average amplitude of mEJPs during 1 minute following 10 Hz stimulation for 10 minutes. (**I**) Number of mEJPs larger than 5 mV during 1 minute following high-frequency stimulation. (**J–P**) FM1-43 dye uptake by control, *shi*^{ts1}, *ΔAB* and full-length rescue larvae after 10 minutes of labeling in high-K^+ solution at 34°C. FM1-43 brightly labels boutons of the NMJ in control and full-length rescue, whereas labeling in *shi*^{ts1} and *ΔAB* is significantly weaker. Note that dye uptake in *ΔAB* NMJs accumulates in the lumen of the bouton (arrow in O), whereas in control (N) and full-length rescue (P) larvae dye is observed close to the bouton perimeter. Dashed lines outline the bouton borders. (**Q**) Quantification of FM1-43 labeling intensity. Bar graphs indicate mean + s.e.m. using Student's *t*-test (B,C,E,H); ANOVA, Bonferroni test (F,I); or ANOVA, Tukey's post test (Q). **P*<0.05, ***P*<0.01, ****P*<0.001. Scale bars: 1 μm.

(Fig. 6J–M,Q). In addition, an increase in the number of internal fluorescent structures was observed (Fig. 6N–P; supplementary material Fig. S5B–D,H,I), suggesting that some of the dye was trapped in large membrane compartments in the terminal. These FM1-43 labeled membrane compartments disappeared when the larvae were returned to 1 mM Ca^{2+} solution and again stimulated with high K^+, supporting the proposition that they are related to the synaptic vesicle cycle (supplementary material Fig. S5E–G).

Subcelluar organization of internal membrane structures in the Dap160 mutant lacking dynamin-binding domains

We next performed electron microscopy to investigate the origin of the internal structures formed during stimulation. Third instar larvae from control, *ΔAB*, *ΔB*, and full-length rescue animals were fixed at rest and after 10 minutes exposure to high potassium. At rest, the morphology of *ΔAB* NMJs is very similar to both control and rescue (Fig. 7A,B; supplementary material Fig. S6A) and the total number of vesicles per terminal is not significantly different (*P*>0.05; Student's *t*-test). However, the packing density of SVs in the distal pool was reduced, while the pool proximal to the T-bar remained unchanged (Fig. 7K). No significant increase in the number of docked vesicles, endocytic pits and endosome-like structures were observed (Fig. 7J,M).

Following stimulation, dramatic structural changes occur in *ΔAB* NMJs. The density and number of SVs in proximal and distal pools is strongly reduced (Fig. 7C,D,L). Numerous large vesicles appear, as verified by serial ultrathin sections. In addition, large bulk membrane invaginations attached to the membrane by tubular connections were observed in the PAZ (Fig. 7D–J). Large vesicles connected by narrow membrane necks to the large membrane invaginations were often seen (Fig. 7E–H). Bulk membrane invaginations were also present in stimulated *ΔB* synapses (supplementary material Fig. S6B).

Surprisingly, no significant difference in the number of coated endocytic pits or collared pits was evident among *ΔAB*, *ΔB*, full-length rescue and control. Coated pits found in synapses from

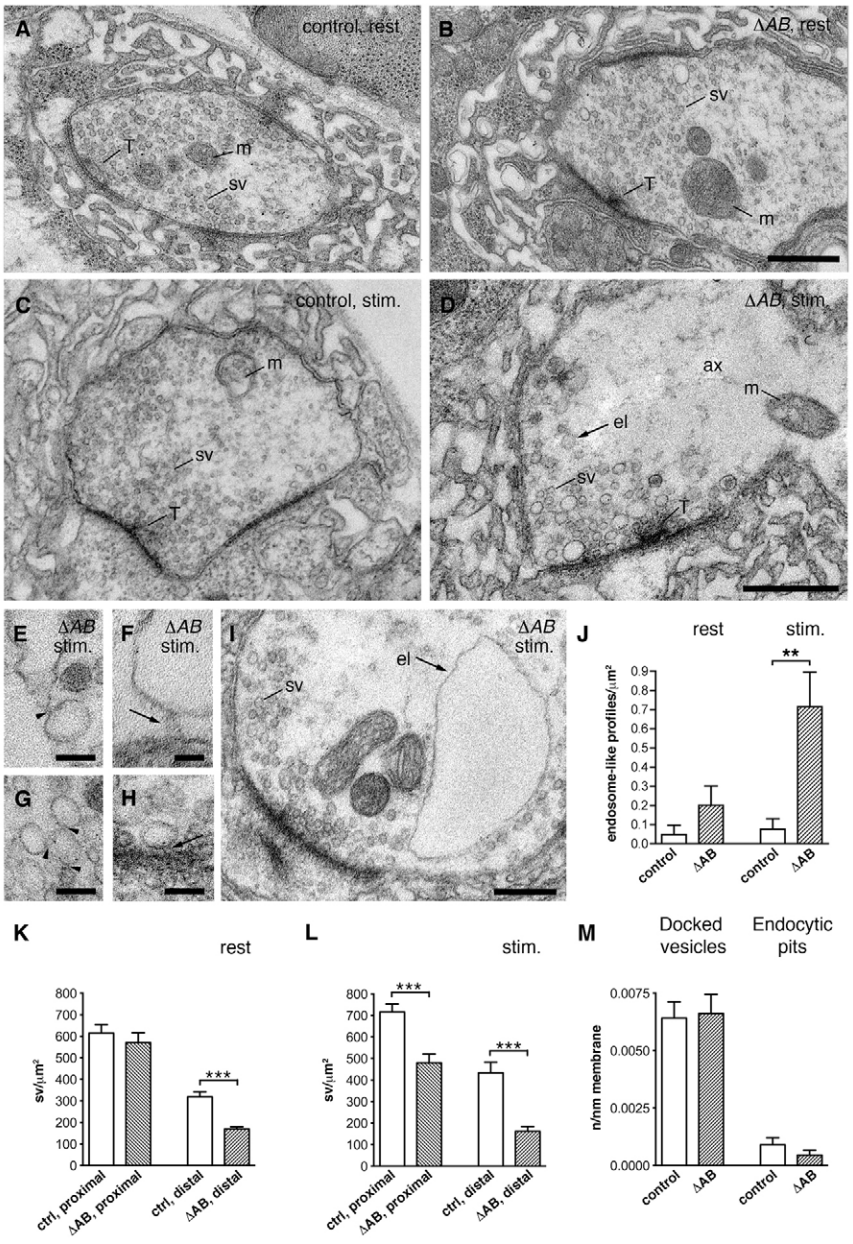

Fig. 7. Decrease in number of synaptic vesicles and accumulation of large endosome-like structures in nerve terminals of *dap160 ΔAB* rescued larvae. (**A**,**B**) Electron micrographs of control (A) and *ΔAB* (B) nerve terminals show that at rest the density of synaptic vesicles is decreased in the distal pool of *ΔAB* nerve terminals (quantified in K). (**C**,**D**) Following high K^+ stimulation at elevated temperature, the number of synaptic vesicles is decreased in both proximal and distal zones in *ΔAB* nerve terminals (quantified in L). Endosome-like profiles are also observed (arrow in D indicates one endosome-like profile). (**E–H**) Higher magnification images show that endosome-like profiles are often connected to each other (arrowheads in E and G) and to the plasma membrane (arrows in F and H). (**I**) Image showing example of large endosome-like structure (arrow). (**J**) The number of large endosome-like profiles (>150 nm) is increased in *ΔAB* following stimulation. (**K,L**) Quantification of synaptic vesicles in the proximal and distal zone at rest (**K**) and following stimulation (**L**). (**M**) The number of docked vesicles and endocytic pits were not significantly different in control and *ΔAB*. T, T-bar; m, mitochondrion; sv, synaptic vesicle; el, endosome-like profile; ax, axoplasm. Bar graphs indicate mean + s.e.m. $^{**}P<0.01$; $^{***}P<0.001$ using Student's *t*-test. Scale bars: 0.5 μm (A–D); 0.1 μm (E,G,H); 25 nm (F); 250 nm (I).

ΔAB, *ΔB*, rescue and control all had a uniform size and did not vary in shape (supplementary material Fig. S6E). This is different from *dap160* null mutant NMJs in which a moderate increase in number of coated pits upon stimulation has been reported (Koh et al., 2004). SVs attached to the active zone by electron dense projections were observed in synapses both in control and mutant NMJs (supplementary material Fig. S6C,D). Tilting the dense protrusions in the electron microscope showed that these electron dense projections are not formed by the plasma membrane, suggesting that they represent docked vesicle assemblies as described in tomographic studies of the cryosubstituted active zones in *Drosophila* (Jiao et al., 2010a) and are therefore not endocytic intermediates. The number of these docked vesicles was not significantly different in stimulated control and *ΔAB* NMJs (Fig. 7M). In summary, EM analysis revealed that deletion of dynamin binding domains in *dap160* leads to severe defects in bulk membrane uptake at the PAZ during high-rate synaptic activity and that the *ΔAB* mutant does not inhibit the fission of clathrin-coated vesicles from the presynaptic membrane.

Discussion

The GTPase dynamin is the key constriction enzyme implicated in the fission reaction during SV membrane recycling at the PAZ. Immunocytochemical studies have localized dynamin to distinct regions at the plasma membrane and to the necks of clathrin-coated pits, thus confirming that dynamin can be membrane associated (Takei et al., 1995). Henceforth, labeling for dynamin has been used as a marker for the PAZ in synapses at rest (Marie et al., 2004; Wagh et al., 2006). Other studies have noted that dynamin localization changes during synaptic activity suggesting that dynamin is associated with an unknown cytoskeletal or 'intravesicular matrix' within the nerve terminal to prevent its

diffusion away from the presynaptic sites (Estes et al., 1996; Pechstein et al., 2010). Using high-resolution techniques we resolved the subcellular origin of this event. Furthermore, we show that dynamin localization in the synapse changes upon activity. A large pool of dynamin is localized in the vesicle cluster at rest and it relocates to the PAZs during synaptic activity. Dap160–dynamin interaction via SH3A-B domains is important for the re-localization and accumulation of dynamin at the PAZ during synaptic activity in *Drosophila* synapses (Fig. 8).

Previous studies have clearly demonstrated that Dap160 also plays an important role in the maintenance of synaptic architecture. In *dap160* mutants, the NMJ displays an increase in small satellite boutons (Koh et al., 2004; Marie et al., 2004), which represent a developmental defect (O'Connor-Giles et al., 2008). In addition, it is also involved in the regulation of dynamin levels at the NMJ during development. Our experiments with *ΔAB* mutants show that the functional endocytic phenotypes can be dissociated from the developmental phenotypes, and moreover the mislocalization of dynamin in *ΔAB* synapses can be separated from the general reduction of dynamin levels in *dap160* null mutants. Our studies show that *ΔAB* boutons display a normal synaptic morphology and maintain the same level of dynamin as control NMJs. We propose that interactions of Dap160 with proteins not involved in SV recycling, in addition to its direct binding to dynamin, accomplish the functions linked to the maturation of the NMJ and ultimately affect dynamin levels in synapses during development. One such binding partner is probably Nervous wreck, which has been shown to interact with the Dap160 SH3C-D domain module (Coyle et al., 2004; O'Connor-Giles et al., 2008). Nervous wreck interacts with dynamin via its SH3A domain (Rodal et al., 2008).

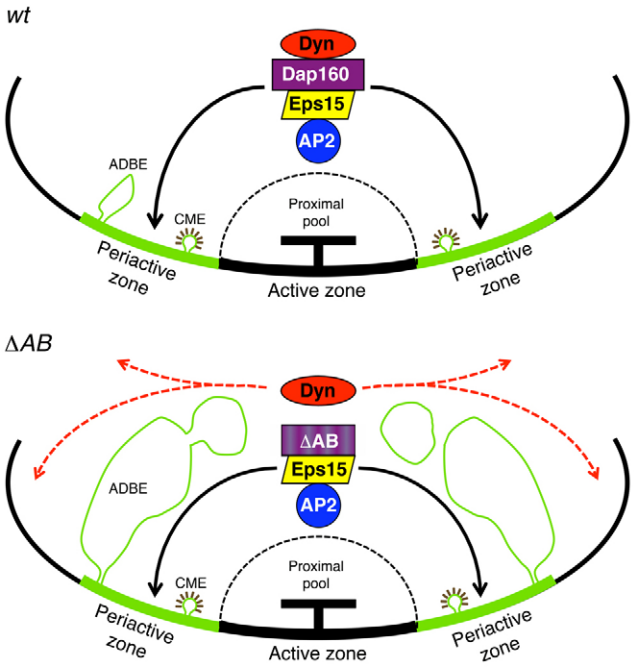

Fig. 8. Scheme of the mechanism for dynamin targeting to the periactive zone during the synaptic vesicle cycle. In wild-type (wt) animals the endocytic proteins AP2, Eps15, Dap160 and dynamin are redistributed from the synaptic vesicle cluster to the periactive zone during intense synaptic activity. Fused synaptic vesicle membrane is recycled by clathrin-mediated endocytosis (CME) and activity-dependent bulk endocytosis (ADBE). In *ΔAB* mutant, dynamin is no longer targeted to the periactive zone, instead it is dispersed in the nerve terminal. Large membrane invaginations and endosome-like structures are accumulated.

The decrease in neurotransmission in *ΔAB* is likely due to the dramatic reduction in the number of synaptic vesicles in nerve terminals upon high-frequency stimulation. Accumulation of membrane invaginations and endosomes suggest that SVs are not properly reformed from the bulk endocytic structures accumulated in NMJs. How does this occur? One possibility is that the block of SV recycling occurs at a step of bulk endocytosis pathway that leads to the formation of SVs. Recent studies suggest that this step may involve clathrin, but contrary to the classical clathrin-mediated pathway it utilizes different adaptor complexes, such as AP1 and AP3 (Cheung and Cousin, 2012). The other non-exclusive possibility is that the classical clathrin-mediated endocytic pathway becomes inhibited at very early step prior to the clathrin recruitment at the PAZ. Our studies show that AP2, Eps15 and Dap160 recruitment to the PAZ is not affected in the mutant. The localization of clathrin, AP1, and AP3 at rest and during stimulation remains to be investigated.

Clathrin-coated pits do not seem affected in *ΔAB* rescue mutants and we did not observe a significant increase when compared to control synapses. The latter supports that dynamin-mediated budding of clathrin-coated pits is not inhibited. This further implies that the targeting of dynamin by Dap160 to the PAZ is not essential for the fission step of the classical clathrin-mediated pathway in *Drosophila* synapses. However, the proper fission of bulk endocytic intermediates is perturbed. The number of uncoated membrane invaginations linked to the presynaptic membrane with thin 'necks' and the number of large interconnected endosomal structures were dramatically increased in the mutants lacking dynamin-binding SH3 domains. Interestingly, it has been noted earlier that appearance of bulk membrane structures in *Drosophila* NMJs occurs in mutants linked to dynamin function or controlling dynamin function upon inactivation of clathrin heavy chain or in clathrin mutants (Kasprowicz et al., 2008). A massive bulk membrane uptake has also been reported in mouse dynamin 1 knockouts (Hayashi et al., 2008). All this supports the hypothesis that dynamin together with clathrin coordinate the balance between clathrin-mediated and bulk endocytosis in synapses.

Large spontaneous EJPs were recorded during the recovery phase following high-rate activity, suggesting that bulk vesicles observed in nerve terminals upon stimulation fuse at the active zone. Disappearance of these large vesicles after cessation of high-frequency stimulation implies that the fused membrane becomes reformed into SVs most probably by clathrin-mediated endocytosis. Fusion of large vesicles will lead to dramatic distortions of quantal release in synapses. Giant fusion events observed in our experiments possibly represent 'traffic accidents', which may have occurred because the scaffolding components controlling bulk membrane trafficking at synapses were imbalanced in the *ΔAB* mutant. This further indicates that the scaffolding function of Dap160/intersectin and proper targeting of dynamin are particularly important for synaptic function during high-rate synaptic activity.

Materials and Methods

Fly stocks and generation of *dap160* transgene and expression constructs

w^{1118} was used as Dap160 wild-type control with the same genetic background as mutants and transgenes and referred to in the text as 'control'. $shibire^{ts1}$ (shi^{ts1}) was obtained from the Bloomington Drosophila Stock Center. $dap160^{\Delta 1}$/*Df(2L)bur-K1* is referred to as *dap160* null is described in Koh et al. (Koh et al., 2004). For rescue experiments the pan-neural driver line *C155-Gal4*; *Df(2L)bur-K1/CyO*, *twi-GFP* were crossed to *UAS-dap160*$^{\Delta B1}$*5C*; $dap160^{\Delta 1}$*/CyO*, *twi-GFP*, or *w*; $dap160^{\Delta 1}$*/CyO*, *twi-GFP*; *UAS-dap160*$^{\Delta AB2}$*8B* or *w*; $dap160^{\Delta 1}$*/CyO*, *twi-GFP*; *UAS-dap160*^{WT} and F1 non-GFP larvae were selected for experiments.

To generate the UAS-rescue constructs with SH3A and SH3B (pUAST-*dap160ΔAB*) or with SH3B (pUAST-*dap160ΔB*) deleted domains, genomic sequence downstream SH3B (nt 3586–4221, FlyBase ID FBgn0023388) was PCR-amplified with forward primers ΔSH3ABf or ΔSH3Bf and reverse primer ΔSH3ABr using the pUAST-*dap160* cDNA plasmid as template. Resulting PCR fragments had 48 nt or 18 nt extensions located 579 nt or 156 nt upstream of amplified region for ΔAB and ΔB, respectively. Restriction sites for sub-cloning are shown in bold letters (supplementary material Table S1). The SpeI–PshAI- or MreI–PshAI-digested PCR fragments were inserted into SpeI– PshAI or MreI–PshAI sites of the pUAST-*dap160*. Resulting plasmids, pUAST-*dap160ΔAB* and pUAST-*dap160ΔB*, have 579 nt or 156 nt deletions comprising SH3AB or SH3B, respectively.

The SH3 expression constructs L1-A-L2, L2-B, AB, ABCD, C, D, and dynamin-PRD in pGEX-6P-2 vector (GE Healthcare) were obtained by PCR using as a template Dap160 cDNA clone IP14822 and *shibire* cDNA clone LD21622 shi, respectively (FlyBase ID FBcl0001466 and FBcl0169663, *Drosophila* Genomics Resource Center, Bloomington, IN) (supplementary material Table S2). The ACD construct was generated by self-ligation of blunt ended PCR product (Fusion polymerase, Finnzyme), amplified from ABCD plasmid. See all primer sequences in supplementary material Table S1. The ACD sequence is identical to one was deleted in the pUAST-*dap160*ΔB. All constructs were verified by sequencing.

GST pull-down

The GST or GST-fusion *dap160*-SH3(L1-A-L2/L2-B/C/D/AB/ACD/ABCD) and GST-fusion dynamin PRD proteins were expressed in BL21(DE3) cells and purified according to standard protocols using glutathione sepharose (GE Healthcare). For GST pull-down 25 μg of corresponding protein were bound to glutathione agarose beads (GE Healthcare), added to 2 mg of *Drosophila* head extract in pull down (PD) buffer (20 mM HEPES, 100 mM KCl, 2 mM $MgCl_2$, 1 mM PMSF, 0.5% Triton X-100) supplemented with Protein Inhibitor Cocktail (Sigma) in a total volume of 0.7 ml. The extracts were incubated on a rotation wheel for 4 hours at 4°C, then washed four times with PD buffer. Protein complexes were eluted with 2× SDS-PAGE sample buffer (Invitrogen) and analyzed by resolving them on a 4–12% SDS-PAGE gel (Invitrogen) and immuno-blotted using specific antibodies.

Antibodies

Polyclonal rabbit and guinea pig Dap160 antisera previously characterized in (Koh et al., 2007) were used in dilutions: 1:500 (rabbit) and 1:1000 (guinea pig). The antisera did not label tissues and NMJs in *dap160* null mutants when stained in parallel with control and $shibire^{ts1}$ (data not shown). A panel of other antibodies was used in the following dilutions: rabbit anti-α-adaptin, AP2, 1:50 (González-Gaitán and Jäckle, 1997); mouse anti-dynamin, 1:300 (clone 41; BD Biosciences); rabbit anti-Dlg, 1:2000 (Cho et al., 2000); mouse anti-Brp, 1:100 (Wagh et al., 2006); mouse anti-CSP mAb 49, 1:50 (Zinsmaier et al., 1994); guinea pig anti-Eps15, 1:1000 (Koh et al., 2007); rabbit anti-synaptotagmin 1:1000 (Littleton et al., 1993). Anti-Brp and AP2 antibodies were kind gifts from E. Buchner (University of Würzburg, Germany) and M. González-Gaitán (Geneva University, Switzerland).

Immunohistochemistry, imaging and quantification of fluorescent image

Labeling of third instar larval fillets was performed as described previously (Verstreken et al., 2008). Secondary antibodies conjugated to Alexa 488, 555 or 647 (Invitrogen) were used at 1:500, secondary antibodies conjugated to Cy5 were used at 1:100 (Invitrogen). Otto dye R1 conjugated secondary antibody was used at dilution 1:100 (Leica). Samples were mounted in Vectashield mounting medium (Vector Laboratories).

STED and confocal microscopy images for Fig. 1D and supplementary material Fig. S1B,C were collected on SP5 confocal microscope system equipped with a STED unit (Leica Microsystems) using 63×oil immersion objective (1.4 NA) and Leica Application Suite Software (Leica Microsystems), which was calibrated to provide resolution up to 70 nm. Other confocal images were captured with 63×, 1.4 NA oil immersion objectives using LSM 510 or a LSM 700 (Carl Zeiss), and the accompanying software. Brightness and contrast were adjusted using ImageJ (http://rsb.info.nih.gov/ij) or Photoshop (Adobe). All measurements were performed in ImageJ or Volocity (PerkinElmer). Volocity was used for evaluating levels of colocalization. Pearson's correlation coefficient was determined for middle optical sections of individual boutons that were selected as Region of Interest. Measurements based on confocal images were from 15 boutons from at least three different animals for each condition and genotype.

Bouton morphology

To reveal bouton outline, third instar larval fillets were labeled with anti-Dlg. Presynaptic T-bars of the active zone were detected by labeling with anti-Brp. Quantification of satellite bouton number was performed according to Marie et al. (Marie et al., 2004). Small boutons that branch from the major NMJ axis or from the terminal bouton were classified as satellite boutons and scored. Confocal images were obtained as described above from NMJ4, segments A2–A5, at an optical section thickness of 0.5 nm. For each genotype 6–9 NMJs from two (*dap160* null) or three (all other genotypes) larvae were analyzed.

Preembedding immunocytochemistry and TEM

Fillets from third instar larvae were prepared in HL3 without Ca^{2+}. For experiments, fillets were incubated in HL3 buffer containing either EDTA for 10 minutes, resting conditions, or stimulated by addition of 60 mM K^+ for 10 minutes. The specimens were fixed in 4% paraformaldehyde solution, in 0.1 M phosphate buffer, pH 7.2 and labeled and embedded for EM as earlier described (Jiao et al., 2010b). Serial ultrathin sections were cut with a diamond knife (Diatome), stained with 1% uranyl acetate and lead citrate on grids, and examined with a Tecnai 12 electron microscope (FEI). Images were quantified using NIH ImageJ software, and statistical evaluation was performed using Excel™ (Microsoft). Relative distribution of gold particles (%) at PAZ or synaptic vesicle pool (SVC) was calculated as the ratio of gold particle density in the PAZ or SVC to the sum of gold particle densities in the SVC and PAZ. PAZ was defined as the plasma membrane area 500 nm adjacent to the active zone and a 100 nm cytosolic space into the lumen from the plasma membrane as shown in supplementary material Fig. S2A. Gold particle density ratio PAZ/outside PAZ was calculated as the ratio of gold particle density in the PAZ to the gold particle density in the area adjacent to PAZ (supplementary material Fig. S2A). At least 10 active zones from three animals were used for quantifications.

3D reconstruction of TEM images

Serial ultrathin sections were photographed using bottom mounted 2k×2k TemCam F224 CCD Camera (TVIPS). Membrane contours were traced using a digitizer and transferred into Maya 8.0® 3D-reconstruction program and surface rendered as earlier described (Jiao et al., 2010b).

Electrophysiology

Third instar larvae were dissected in Ca^{2+} free HL3 solution as described previously (Koh et al., 2007). mEJPs were recorded from muscle 6 or 7 in segment A3 with thin-walled micropipettes filled with 3 M KCl in HL3 solution containing 1 mM $CaCl_2$ (Hallermann et al., 2010). A suction electrode backfilled with HL3 solution was used to stimulate motor axons innervating the muscles. Low frequency stimulation was applied at 0.3 Hz, high frequency at 10 Hz. Data were recorded using an Axoclamp 2B amplifier, and ClampFit v10 software running on a PC computer equipped with an A/D interface (Axon Instruments) was used for data collection. Recordings were used in analysis only when the membrane potential was above 60 mV for mEJP measurement and for evoked EJPs when the membrane potential fell by less than 10 mV during the recording period. mEJPs were quantified for frequency and amplitude by taking the average value during 1 min for a minimum of five traces. Evoked EJPs were analyzed by calculating the average amplitude of 10 EJPs per every minute bin of 10 Hz stimulation for five or more recordings. Recovery from stimulation was analyzed by measuring the amplitude of six EJPs evoked at 0.3 Hz following 4 minutes, 10 Hz stimulation for five traces. All recordings were analyzed using Clampfit v10 software and data processed using Graph Pad Prism v5. Recordings were from 5–11 animals per genotype and condition.

FM1-43 dye uptake

FM1-43 dye uptake experiments were performed as described by Verstreken et al. (Verstreken et al., 2008). For each experiment one control and one test larva were dissected on small Sylgard plates and incubated in HL3 with 60 mM KCl and 4 μM FM1-43 (Invitrogen) back to back in a 1.5 ml Eppendorf tube for 10 minutes in a 34°C waterbath. Excess dye was then washed away repeatedly with Ca^{2+}-free HL3 solution over 15 minutes. For unloading experiments larval fillets was instead washed with HL3 solution containing 1 mM Ca^{2+} and then again stimulated with high K^+ except this time without FM1-43 dye, and then subjected to washing with Ca^{2+}-free HL3 solution. Labeling was captured with a 40×water immersion objective (NA 1.0) on a LSM 700 (Carl Zeiss). Data acquisition as well as data processing and quantification were performed as described (Verstreken et al., 2008). Three animals per genotype were tested in dye uptake experiments. To test dye unloading two separate experiments for each genotype were carried out.

Larval locomotion assay

Larval locomotion was tested according to Yang et al. (Yang et al.). Briefly, individual third instar larvae were placed in the centre of Petri dishes (8.5 cm diameter, 1.5 cm height) coated with 1% agarose. Distance travelled by each larva during a 3-minute period was measured by placing the Petri dish over a grid of

25 mm^2 squares and scoring the number of grid squares entered. Larval locomotion was tested at 25℃ and 34℃. At elevated temperature the larvae were preheated for 10 minutes on preheated yeast-supplemented apple juice agar plates in humidified chambers before locomotion was tested. For each genotype and condition 24–27 larvae were tested.

Statistics

Statistical analysis of two groups was evaluated using Student's *t*-tests. To evaluate the differences between more than two groups one-way analysis of variance (ANOVA) was used, either with Tukey's post-test, comparing every mean with every other mean, or Bonferroni multiple comparison test, comparing selected pairs of means. Statistical analysis was performed using GraphPad Prism v5.0 or v6.0 (GraphStat Software, San Diego, CA). Non-significant differences are not indicated in figures.

Acknowledgements

We thank E. Buchner, M. González-Gaitán and the University of Iowa Hybridoma Bank for antibodies.

Author contributions

Å.M.E.W., O.V., K.A.R., T.W.K., H.J.B. and O.S. designed experiments; Å.M.E.W., W.J., O.V., K.A.R., E.S., K.L.S. and O.S. performed experiments; Å.M.E.W., W.J., O.V., K.A.R., E.S. and O.S. analyzed data; all authors discussed the data and commented on the manuscript; Å.M.E.W. and O.S. wrote the manuscript.

Funding

This work was supported by the Swedish Research Council [grant numbers 13473 and 529-2009-6646/ESF-Euromembrane] and Linné Center DBRM; the European Union Seventh Framework Programme (SynSys-project) [grant agreement number HEALTH-F2-2009-242167]; and the Wallenberg Foundation and Hjärnfonden (to O.S.). H.J.B. is an investigator of the Howard Hughes Medical Institute.

Supplementary material available online at
http://jcs.biologists.org/lookup/suppl/doi:10.1242/jcs.118968/-/DC1

References

Broadie, K. (2004). Synapse scaffolding: intersection of endocytosis and growth. *Curr. Biol.* **14**, R853-R855.

Cheung, G. and Cousin, M. A. (2012). Adaptor protein complexes 1 and 3 are essential for generation of synaptic vesicles from activity-dependent bulk endosomes. *J. Neurosci.* **32**, 6014-6023.

Cho, K. O., Chern, J., Izaddoost, S. and Choi, K. W. (2000). Novel signaling from the peripodial membrane is essential for eye disc patterning in Drosophila. *Cell* **103**, 331-342.

Coyle, I. P., Koh, Y. H., Lee, W. C., Slind, J., Fergestad, T., Littleton, J. T. and Ganetzky, B. (2004). Nervous wreck, an SH3 adaptor protein that interacts with Wsp, regulates synaptic growth in Drosophila. *Neuron* **41**, 521-534.

Dittman, J. and Ryan, T. A. (2009). Molecular circuitry of endocytosis at nerve terminals. *Annu. Rev. Cell Dev. Biol.* **25**, 133-160.

Estes, P. S., Roos, J., van der Bliek, A., Kelly, R. B., Krishnan, K. S. and Ramaswami, M. (1996). Traffic of dynamin within individual Drosophila synaptic boutons relative to compartment-specific markers. *J. Neurosci.* **16**, 5443-5456.

Evergren, E., Gad, H., Walther, K., Sundborger, A., Tomilin, N. and Shupliakov, O. (2007). Intersectin is a negative regulator of dynamin recruitment to the synaptic endocytic zone in the central synapse. *J. Neurosci.* **27**, 379-390.

Ferguson, S. M. and De Camilli, P. (2012). Dynamin, a membrane-remodelling GTPase. *Nat. Rev. Mol. Cell Biol.* **13**, 75-88.

González-Gaitán, M. and Jäckle, H. (1997). Role of Drosophila alpha-adaptin in presynaptic vesicle recycling. *Cell* **88**, 767-776.

Hallermann, S., Heckmann, M. and Kittel, R. J. (2010). Mechanisms of short-term plasticity at neuromuscular active zones of Drosophila. *HFSP J.* **4**, 72-84.

Hayashi, M., Raimondi, A., O'Toole, E., Paradise, S., Collesi, C., Cremona, O., Ferguson, S. M. and De Camilli, P. (2008). Cell- and stimulus-dependent heterogeneity of synaptic vesicle endocytic recycling mechanisms revealed by studies of dynamin 1-null neurons. *Proc. Natl. Acad. Sci. USA* **105**, 2175-2180.

Henne, W. M., Boucrot, E., Meinecke, M., Evergren, E., Vallis, Y., Mittal, R. and McMahon, H. T. (2010). FCHo proteins are nucleators of clathrin-mediated endocytosis. *Science* **328**, 1281-1284.

Jiao, W., Masich, S., Franzén, O. and Shupliakov, O. (2010a). Two pools of vesicles associated with the presynaptic cytosolic projection in Drosophila neuromuscular junctions. *J. Struct. Biol.* **172**, 389-394.

Jiao, W., Shupliakov, A. and Shupliakov, O. (2010b). A semi-correlative technique for the subcellular localization of proteins in Drosophila synapses. *J. Neurosci. Methods* **185**, 273-279.

Kasprowicz, J., Kuenen, S., Miskiewicz, K., Habets, R. L., Smitz, L. and Verstreken, P. (2008). Inactivation of clathrin heavy chain inhibits synaptic recycling but allows bulk membrane uptake. *J. Cell Biol.* **182**, 1007-1016.

Koenig, J. H. and Ikeda, K. (1989). Disappearance and reformation of synaptic vesicle membrane upon transmitter release observed under reversible blockage of membrane retrieval. *J. Neurosci.* **9**, 3844-3860.

Koh, T. W., Verstreken, P. and Bellen, H. J. (2004). Dap160/intersectin acts as a stabilizing scaffold required for synaptic development and vesicle endocytosis. *Neuron* **43**, 193-205.

Koh, T. W., Korolchuk, V. I., Wairkar, Y. P., Jiao, W., Evergren, E., Pan, H., Zhou, Y., Venken, K. J., Shupliakov, O., Robinson, I. M. et al. (2007). Eps15 and Dap160 control synaptic vesicle membrane retrieval and synapse development. *J. Cell Biol.* **178**, 309-322.

Littleton, J. T., Bellen, H. J. and Perin, M. S. (1993). Expression of synaptotagmin in Drosophila reveals transport and localization of synaptic vesicles to the synapse. *Development* **118**, 1077-1088.

Marie, B., Sweeney, S. T., Poskanzer, K. E., Roos, J., Kelly, R. B. and Davis, G. W. (2004). Dap160/intersectin scaffolds the periactive zone to achieve high-fidelity endocytosis and normal synaptic growth. *Neuron* **43**, 207-219.

O'Connor-Giles, K. M., Ho, L. L. and Ganetzky, B. (2008). Nervous wreck interacts with thickveins and the endocytic machinery to attenuate retrograde BMP signaling during synaptic growth. *Neuron* **58**, 507-518.

Pechstein, A., Shupliakov, O. and Haucke, V. (2010). Intersectin 1: a versatile actor in the synaptic vesicle cycle. *Biochem. Soc. Trans.* **38**, 181-186.

Rodal, A. A., Motola-Barnes, R. N. and Littleton, J. T. (2008). Nervous wreck and Cdc42 cooperate to regulate endocytic actin assembly during synaptic growth. *J. Neurosci.* **28**, 8316-8325.

Roos, J. and Kelly, R. B. (1998). Dap160, a neural-specific Eps15 homology and multiple SH3 domain-containing protein that interacts with Drosophila dynamin. *J. Biol. Chem.* **273**, 19108-19119.

Roos, J. and Kelly, R. B. (1999). The endocytic machinery in nerve terminals surrounds sites of exocytosis. *Curr. Biol.* **9**, 1411-1414.

Saheki, Y. and De Camilli, P. (2012). Synaptic vesicle endocytosis. *Cold Spring Harb. Perspect. Biol.* **4**, a005645.

Takei, K., McPherson, P. S., Schmid, S. L. and De Camilli, P. (1995). Tubular membrane invaginations coated by dynamin rings are induced by GTP-gamma S in nerve terminals. *Nature* **374**, 186-190.

Verstreken, P., Ohyama, T. and Bellen, H. J. (2008). FM 1-43 labeling of synaptic vesicle pools at the Drosophila neuromuscular junction. *Methods Mol. Biol.* **440**, 349-369.

Wagh, D. A., Rasse, T. M., Asan, E., Hofbauer, A., Schwenkert, I., Dürrbeck, H., Buchner, S., Dabauvalle, M. C., Schmidt, M., Qin, G. et al. (2006). Bruchpilot, a protein with homology to ELKS/CAST, is required for structural integrity and function of synaptic active zones in Drosophila. *Neuron* **49**, 833-844.

Yang, P., Shaver, S. A., Hilliker, A. J. and Sokolowski, M. B. (2000). Abnormal turning behaviour in Drosophila larvae: Identification and molecular analysis of scribbler (sbb). *Genetics* **155**, 1161-1174.

Zinsmaier, K. E., Eberle, K. K., Buchner, E., Walter, N. and Benzer, S. (1994). Paralysis and early death in cysteine string protein mutants of Drosophila. *Science* **263**, 977-980.